

Skyrmionic spin structures in layered Fe_5GeTe_2 up to room temperature

Maurice Schmitt¹, Thibaud Denneulin², András Kovács², Tom G. Saunderson^{1,3}, Philipp Rößmann^{3,4}, Aga Shahee^{1,10}, Tanja Scholz⁵, Amir H. Tavabi², Martin Gradhand^{1,6}, Phivos Mavropoulos⁷, Bettina V. Lotsch^{5,8}, Rafal E. Dunin-Borkowski², Yuriy Mokrousov^{1,3}, Stefan Blügel³ & Mathias Kläui^{1,9}✉

The role of the crystal lattice, temperature and magnetic field for the spin structure formation in the 2D van der Waals magnet Fe_5GeTe_2 with magnetic ordering up to room temperature is a key open question. Using Lorentz transmission electron microscopy, we experimentally observe topological spin structures up to room temperature in the metastable pre-cooling and stable post-cooling phase of Fe_5GeTe_2 . Over wide temperature and field ranges, skyrmionic magnetic bubbles form without preferred chirality, which is indicative of centrosymmetry. These skyrmions can be observed even in the absence of external fields. To understand the complex magnetic order in Fe_5GeTe_2 , we compare macroscopic magnetometry characterization results with microscopic density functional theory and spin-model calculations. Our results show that even up to room temperature, topological spin structures can be stabilized in centrosymmetric van der Waals magnets.

¹Johannes Gutenberg Universität Mainz, Institut für Physik, Staudingerweg 7, 55128 Mainz, Germany. ²Ernst Ruska-Centre for Microscopy and Spectroscopy with Electrons and Peter Grünberg Institute, Forschungszentrum Jülich, 52425 Jülich, Germany. ³Peter Grünberg Institut and Institute for Advanced Simulation, Forschungszentrum Jülich, 52425 Jülich, Germany. ⁴Institute of Theoretical Physics and Astrophysics, University of Würzburg, Am Hubland, 97074 Würzburg, Germany. ⁵Max Planck Institute for Solid State Research, Heisenbergstraße 1, 70569 Stuttgart, Germany. ⁶University of Bristol, School of Physics, HH Wills Physics Laboratory, Tyndall Avenue, Bristol BS8 1TL, England. ⁷National and Kapodistrian University of Athens, Department of Physics, University Campus, GR-157 84 Zografou, Athens, Greece. ⁸Department of Chemistry, University of Munich (LMU), Butenandtstraße 5-13 (Haus D), 81377 München, Germany. ⁹QuSpin, Department of Physics, Norwegian University of Science and Technology, NTNU, NO-7491 Trondheim, Norway. ¹⁰Present address: Centre for Interdisciplinary Research & Innovations, University of Kashmir, Hazratbal, Srinagar, Jammu and Kashmir 190006, India. ✉email: klaeui@uni-mainz.de

Two-dimensional (2D) magnetic van der Waals (vdW) materials have seen rising attention since their recent introduction into the field of spintronics and beyond¹. Many of these materials show promising properties for future applications, such as the semiconducting 2D ferromagnet CrI₃², the metallic 2D ferromagnet Fe₃GeTe₂³ and the very recently discovered metallic 2D ferromagnet Fe₅GeTe₂ that orders even at relatively high temperatures^{4,5}. Not only has its magnetic order exhibited significant complexity⁶, the closely related material (Fe_{0.5}Co_{0.5})₅GeTe₂, whose magnetic order exists at room temperature^{7,8}, has already been shown to host skyrmions⁹. The operation of a spintronic device requires ferromagnetic materials with room-temperature magnetic ordering, but most of the 2D vdW magnetic materials are either not ferromagnetic or do not possess a high magnetic ordering temperature. Here, Fe₅GeTe₂ is unique in that it has attracted specific scientific attention due to its room-temperature ferromagnetism with an ordering temperature of $T_C \approx 310$ K. To make use of a magnetic system for applications, spin structures are often required as information carriers. Interest in the dynamics of spin structures accordingly motivated recent studies on domain walls in vdW magnets^{10,11}. A particularly promising and exciting spin structure is the magnetic skyrmion^{12–14}, which has also been observed in the related material Fe₃GeTe₂^{15,16}. Hence, for 2D magnet applications, the required next step is the observation of topological magnetic spin structures near room temperature in Fe₅GeTe₂. Recently, meron spin structures have been observed in domain walls of Fe₅GeTe₂, but they could only be stabilized well below room temperature¹⁷. Fe₅GeTe₂ is additionally intriguing as it exhibits an irreversible magneto-structural phase transition upon cooling below ≈ 100 K for the first time after synthesization of quenched Fe₅GeTe₂ crystals¹⁸. This means that Fe₅GeTe₂ crystals, which have been quenched to room temperature in the synthesization process remain in a metastable phase at room temperature before reaching a stable phase after cooling below ≈ 100 K for the first time. Upon heating back up to higher temperatures even above room temperature, Fe₅GeTe₂ remains in this magneto-structural phase, thus indicating the thermal stability of this phase. There is particular interest in the spin structures in a Fe₅GeTe₂ crystal, before and after going through the irreversible phase transition upon cooling below $T \approx 100$ K. These phases are termed the metastable pre-cooling and the stable post-cooling phases. Real space probing of the crystal lattice and spin structure in both of these phases is still a major open question.

In the present work, bulk magnetic properties in the phases of 2D Fe₅GeTe₂ are characterized using a superconducting quantum interference device (SQUID), in combination with magnetic domain images using Lorentz transmission electron microscopy (L-TEM), which reveals stable topological spin structures up to room temperature. Further, the crystallographic space groups previously suggested for Fe₅GeTe₂ are investigated and we resolve open questions about their symmetry by presenting a spin chirality analysis. The spin chirality analysis involves careful considerations of the chirality of observed spin structures in Fe₅GeTe₂, in order to deduce if the chiral Dzyaloshinskii-Moriya interaction (DMI) is present in the sample. Finally, the complex magnetic ordering of Fe₅GeTe₂ is closely examined and we determine that the system is not in a spin glassy state. This is done via a careful comparison of the effective anisotropy obtained on a macroscopic scale with the effective anisotropy obtained on a microscopic scale.

Results and discussion

Structural and composition analysis. Figure 1(a) shows a cross-section atomic resolution high angle annular dark-field detector

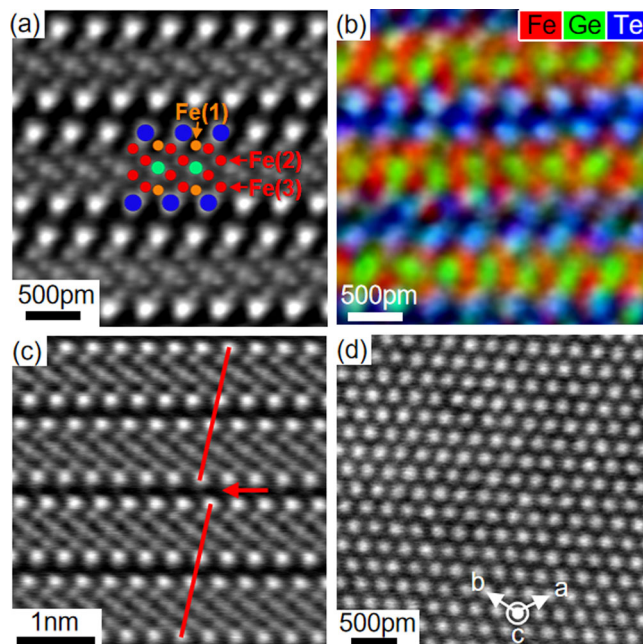


Fig. 1 High resolution analyses of the crystal structure of Fe₅GeTe₂.

a High resolution high angle annular dark-field detector (HAADF) scanning transmission electron microscopy (STEM) image of the structure with the *c*-axis along the vertical direction in the image plane. **b** Color-coded energy dispersive X-ray (EDX) composition map showing the distribution of iron, germanium and tellurium. A schematic model of the atomic structure is overlaid on image (a) with the same color code as in panel **b**. **c** HAADF STEM image showing a stacking fault as indicated by red lines and an arrow. **d** HAADF STEM image of the structure with the *c*-axis perpendicular to the image plane.

(HAADF) scanning transmission electron microscopy (STEM) image of the quenched single-crystal Fe₅GeTe₂ used in the present work. Figure 1(b) is a color-coded composition map obtained using energy dispersive X-ray (EDX) spectroscopy, which shows the periodic distribution of iron, germanium and tellurium. 2D layers consist of a sandwich of two planes of Te (brightest columns) with Ge and Fe planes located in-between. The layers are stacked along the *c*-axis and are approximately 1 nm thick including the vdW gap (dark area between two neighboring Te planes). A schematic model of the atomic structure is overlaid in the middle of Fig. 1(a) with the same color code as in Fig. 1(b). Following the notation used by May et al.⁴, the Fe(2) and Fe(3) columns can be identified but the Fe(1) columns are not visible. Since STEM images show a projection of the crystal structure over the thickness of the lamella, this iron site is not easily visible because of its split-site nature⁴. Figure 1(c) is another HAADF STEM that shows the presence of a stacking fault as indicated by red lines and an arrow, which has been previously reported in Fe₅GeTe₂¹⁹. Here, stacking faults were observed primarily near the surface of the crystal (down to 200 nm below the surface). They are scarce deeper in the bulk of the sample, which has essentially a regular crystal structure, as shown in Fig. 1(a). Figure 1(d) is a plan-view image where the *c*-axis is perpendicular to the image, which shows the hexagonal shape of the lattice.

Magnetic imaging of skyrmionic spin structures. We first observe the magnetization configuration at room temperature in our sample in the pre-cooling phase, as the types of spin structures also entail information about the underlying crystal structure of Fe₅GeTe₂. The space group of Fe₅GeTe₂ has not so far

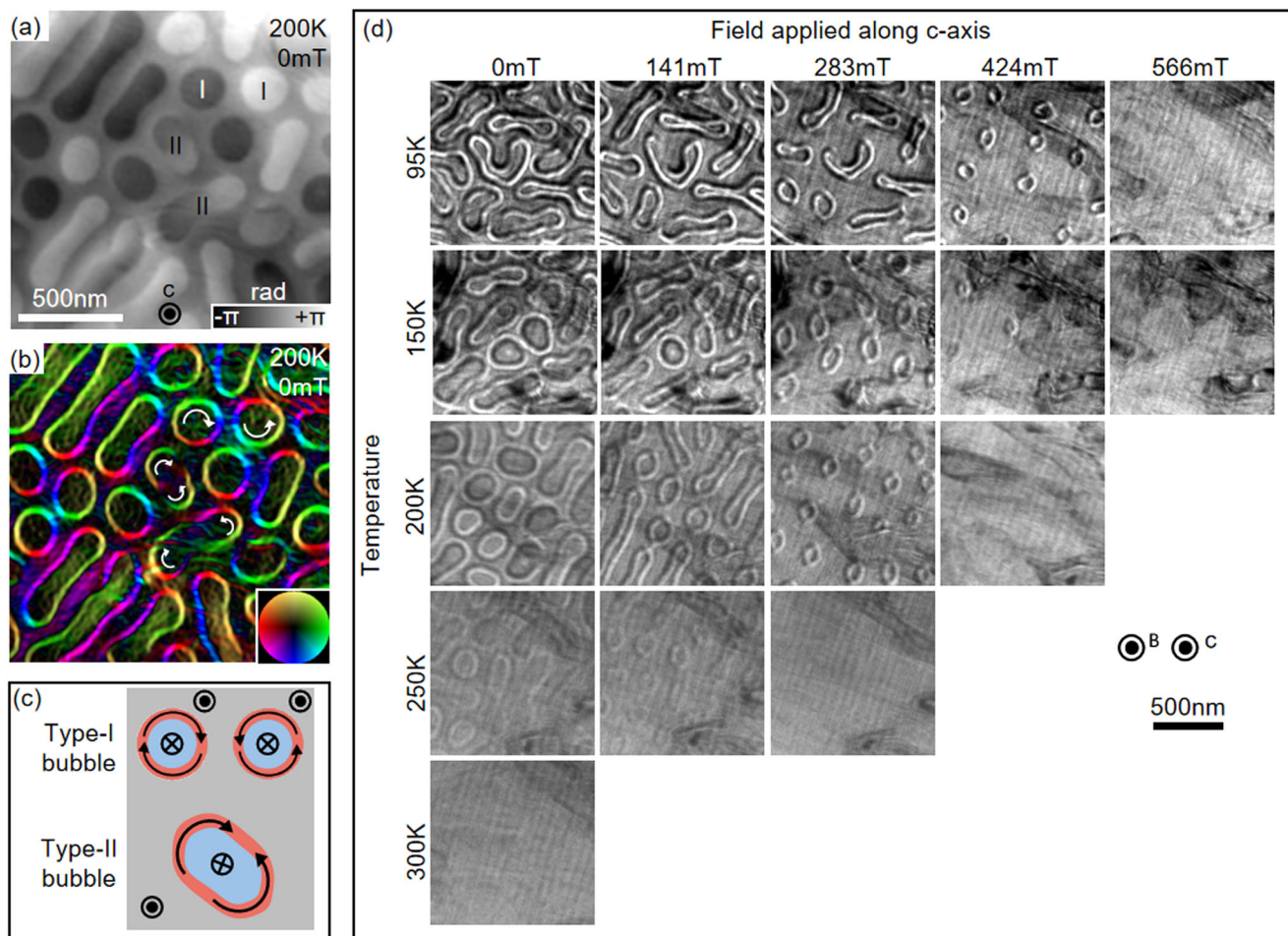


Fig. 2 Magnetic imaging of Fe_5GeTe_2 in the pre-cooling phase, revealing skyrmionic spin structures. **a** Phase shift image obtained using off-axis electron holography at $T = 200\text{ K}$ and $B = 0\text{ mT}$ in Fe_5GeTe_2 with the c -axis perpendicular to the image plane after previously applying out-of-plane fields up to $B = 566\text{ mT}$. **b** Corresponding color-coded magnetic induction map where the direction of the magnetic field is given by the color wheel. Type-II as well as type-I bubbles with opposite winding numbers are present. **c** Schematic illustration of type-I and type-II bubbles. **d** Series of Fresnel images taken at various temperatures and external out-of-plane fields (parallel to the c -axis) with a defocus of -1 mm , in a $\approx 100\text{ nm}$ thick plan-view lamella (c -axis is perpendicular to the image plane). The magnetization within the magnetic bubbles opposes the external field, whereas the areas the magnetization between the bubbles are parallel to the field. Bubbles begin to form at higher external fields for lower temperatures.

been identified unambiguously. Li et al. and May et al. report the centrosymmetric space group $R\bar{3}m$ (No. 166)^{4,20}, whereas Stahl et al. reported the non-centrosymmetric space group $R3m$ (No. 160)¹⁹. Here we consider the skyrmionic spin structures in Fe_5GeTe_2 to resolve this space group issue. A prerequisite for chiral spin structures, such as skyrmions and chiral domain walls, is the DMI, which occurs in systems with broken inversion symmetry²¹. In this regard, chiral spin structures would not be stabilized in bulk Fe_5GeTe_2 if its space group is $R\bar{3}m$, whereas they could be stabilized in bulk Fe_5GeTe_2 with the non-centrosymmetric space group $R3m$.

Figure 2(a, b) show an in-focus phase shift image and the corresponding magnetic induction map reconstructed from an off-axis electron hologram obtained in a lamella cut perpendicular to the c -axis. The sample is magnetized along the crystallographic c -axis, which can also be deduced from SQUID measurements, as discussed in section Supplementary Note 1 and shown in Supplementary Fig. S1 of the supplementary information. Two different types of circular spin structures can be observed. These bubbles with a black or white electron phase contrast correspond to type-I bubbles with a clockwise or counter-clockwise field rotation²². These two possible chiralities were found to occur with equal probabilities. Bubbles that show a

black to white phase gradient correspond to topologically trivial type-II bubbles in which the rotation of the field changes²². Figure 2(c) shows schematically the magnetic field in type-I and type-II bubbles. The presence of both type-II and type-I bubbles with two possible chiralities indicate that they are not stabilized by bulk DMI²³, but likely by dipolar interactions. We give further reasoning for our conclusion that these bubbles are likely stabilized by dipolar interactions in the supplementary section Supplementary Note 6 and Supplementary Fig. S5. Furthermore, all observed bubbles are Bloch-type bubbles, as can be seen in Fig. 2b, which is an indication that no significant interfacial DMI is present in our Fe_5GeTe_2 sample either²⁴. These observations are indicative of underlying centrosymmetry and thus support the results of Li et al. and May et al. regarding the centrosymmetric space group $R\bar{3}m$ for Fe_5GeTe_2 ^{4,20}. It is worth noting that the L-TEM samples used here have been cut such that the stacking faults observed near the surface of bulk samples are not present. While additional stacking faults can occur during the phase transition, as shown in supplementary section Supplementary Note 8, Supplementary Fig. S7 and Supplementary Fig. S8, the images in Fig. 2 are recorded in the pre-cooling phase, such that symmetry breaking due to stacking faults is expected to be negligible.

A series of Fresnel defocus images taken at different temperatures and external fields, as shown in Fig. 2(d), reveals that the formation of bubbles is favorable over labyrinth domains at larger applied fields, and that the bubbles form at fields slightly smaller than the saturating fields at any temperature. This is in line with previous results on other systems, where it was shown that skyrmion formation can be favorable at sufficiently strong external fields²⁵. Furthermore, we observe that the sizes of the magnetic bubbles shrink as the opposing net magnetization grows with external field, which is also in line with previous reports for chiral skyrmions and non-chiral skyrmions^{22,26}. In the individual field sweeps shown in Fig. 2(d), the sample is previously saturated along the positive field direction, then the external field is turned off and finally the field sweep is done from zero field until the sample saturates again at a high positive field. In this case, bubbles are stabilized even at zero external field, since the external field gradually ramps down from the saturation field, nucleating bubbles slightly below the saturation field. With this history, even when zero external field is reached, a transformation to e.g., stripe domains is not observed.

Pre-cooling and post-cooling magnetic properties. In order to explore the bulk magnetic properties of quenched Fe₅GeTe₂ in both the metastable pre-cooling and stable post-cooling phases, we have taken SQUID measurements of our sample while it is going through the phase transition. With SQUID the magnetization of bulk Fe₅GeTe₂ can be measured quantitatively and quickly, which is not possible with L-TEM. The temperature dependence of the magnetization for two magnetic field directions, B parallel to the ab-plane ($B_{ab\text{-plane}}$) and B parallel to the c-axis ($B_{c\text{-axis}}$) in an external field of 0.1 T for Fe₅GeTe₂ is shown in Fig. 3(a) and (b), respectively. For $B_{ab\text{-plane}}$, the first Field Cooled Cooling (FCC₁) curve reveals three magnetic anomalies. The anomaly at 271 K corresponds to the magnetic ordering temperature (T_C). The anomaly related to decreasing magnetization at 136 K (T_{C2}) may correspond to a transition to a spin glassy phase²⁷. Another possible explanation is that Fe₅GeTe₂ may be in a ferrimagnetic order under these conditions, as previously suggested for a similar temperature range by Ohta et al. and Alahmed et al., respectively^{28,29}. However, as soon as our sample reaches the stable post-cooling phase, it is found to be in a ferromagnetic state. Finally, the anomaly of a sudden increase in magnetization at $T=87$ K corresponds to an irreversible magneto-structural phase transition (T_S) from a metastable pre-cooling phase to a stable post-cooling phase, consistent with previous results^{4,19}. In the Field Cooled Warming (FCW) curve and the FCC₂ curve, no such anomaly is evident at ≈ 100 K, thus confirming the 87 K anomaly of FCC₁ data was due to the non-reversible nature of this magneto-structural phase transition. While a weak anomaly with an increase in magnetization is evident at 118 K in FCW followed by a narrow hysteresis between FCW and FCC₂, it may be due to some spin reoriented phase transition. Further, the critical temperature T_C has shifted from 270 K to 310 K. Such a shift in T_C is consistent with previous reports¹⁸. The difference in the net magnetization between 100 K to 300 K for FCW and FCC₁ curves may be partially caused by the two different spin textures that Fe₅GeTe₂ exhibits between the stable post-cooling and the metastable pre-cooling phases, which will be discussed later in more detail.

Due to the irreversibility of the phase transition that occurs at 87 K, newly synthesized crystal pieces were chosen for the $B_{c\text{-axis}}$ measurements. The $B_{c\text{-axis}}$ data curves show similar magnetic behavior to that of the $B_{ab\text{-plane}}$ configuration. The slightly different values of T_{C2} and T_S for the $B_{ab\text{-plane}}$ and $B_{c\text{-axis}}$ FCC curves may be due to the magneto-crystalline anisotropy. That T_C

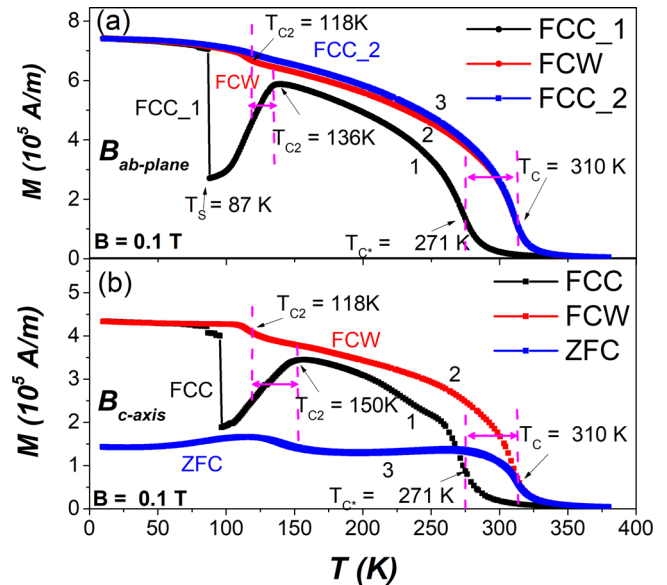


Fig. 3 Magnetization vs. temperature of Fe₅GeTe₂. The external field B is applied along the c-axis and in the ab-plane with a field strength of 0.1 T, while the temperature T is varied and the magnetization M is measured. Zero field cooled (ZFC) indicates that the sample was cooled without application of an external field and then the field of 0.1 T was applied at the lowest temperature followed by measurements performed during warming. Field cooled cooling (FCC) and field cooled warming (FCW) indicates measurements performed subsequently during cooling and warming with the field kept on, respectively. The numbers 1, 2, 3 define the measurement sequence. When the external magnetic field is in the ab-plane (a), the sequence is FCC₁, followed by FCW and finally FCC₂, while for B along the c-axis (b), the sequence is FCC followed by FCW and finally ZFC. T_C denotes the critical temperature associated with the phase transition to the paramagnetic phase and at T_{C2} the magnetization starts to exhibit its characteristic behavior. The standard deviation of each data point is smaller than 100 A/m and as such smaller than the displayed markers.

is almost the same value in both configurations further indicates that the magneto-crystalline anisotropy is a possible origin of the observed difference in T_{C2} and T_S for the two measurement configurations. The third and final curve is a zero-field cooled (ZFC) curve, which also shows a T_C of 310 K with low net magnetization. The large difference between the ZFC and FCW curves may have resulted from the occurrence of different domain configurations due to the external magnetic field-induced reorientation of ferromagnetic components. Consequently, the characteristic properties of the M-T curve are observed in two independent samples, once when a field is applied along the c-axis, and once when the field is applied perpendicular to the c-axis.

In Fig. 4, one can quantitatively see an increase in magnetization in the post-cooling phase compared to the pre-cooling phase under otherwise equivalent conditions. This is true for the wide range of measured temperatures and external fields, in both the $B_{c\text{-axis}}$ and $B_{ab\text{-plane}}$ configurations. For example, at 150 K and 100 mT in the $B_{ab\text{-plane}}$ configuration:

$$M_{\text{pre-cooling}}^{150\text{K}}(B = 100 \text{ mT}) = (5.75 \pm 0.12) \cdot 10^5 \text{ A m}^{-1}, \quad (1)$$

$$M_{\text{post-cooling}}^{150\text{K}}(B = 100 \text{ mT}) = (6.54 \pm 0.13) \cdot 10^5 \text{ A m}^{-1}. \quad (2)$$

The SQUID measurements yielded a saturation magnetization of

$$M_s = (8.12 \pm 0.16) \cdot 10^5 \text{ A m}^{-1}. \quad (3)$$

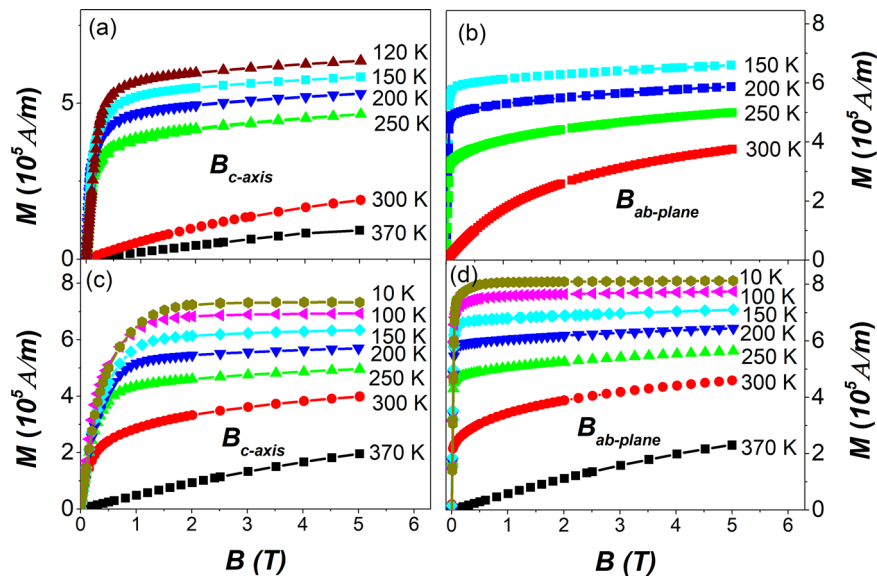


Fig. 4 Magnetic field dependent magnetization curves. The external field B is applied along the c -axis and in the ab -plane at different temperatures, while the magnetization M is measured. **a, b** for the pre-cooling and **c, d** for the post-cooling phase. The standard deviation of each data point is smaller than 100 A/m and as such smaller than the displayed markers.

To confirm the validity of this saturation magnetization value, an independent method to determine the saturation magnetization via analysis of the stripe domain patterns is used³⁰. The resulting value is $M_s = (2.56 \pm 1.40) \cdot 10^6 \text{ A m}^{-1}$. This value has a relatively large uncertainty, and the method neglects e.g., shape anisotropy and surface defects. However, it is sufficiently close to the saturation magnetization measured with the SQUID and thus confirms its validity. The details of the method and calculation can be found in section Supplementary Note 2 and Supplementary Fig. S2 of the supplementary information.

At this point, it is worth noting that the M-H curve at 120 K in the pre-cooling phase shown in Fig. 4(a) is in line with the other recorded curves. This suggests that the decreasing magnetization with decreasing temperature observed in this regime in Fig. 3 is not due to a spin glassy state³¹. This is in line with results discussed later in this paper, where the magnetic ordering of Fe_5GeTe_2 is discussed and it is found that Fe_5GeTe_2 is not in a spin glassy state using an independent method.

Finally, we have taken a series of Fresnel defocus images of our sample at temperatures ranging from 95 K to 290 K and at a constant external field of $B = 100 \text{ mT}$ along the c -axis, both in the pre-cooling and post-cooling phases. The phase transition from the metastable pre-cooling to the stable post-cooling phase in the TEM lamellae was achieved by cooling the sample down to $\approx 77 \text{ K}$, leaving it in liquid nitrogen for one hour. The images for these temperature sweeps are shown in Fig. 5. Furthermore, a direct comparison of field sweeps at both phases is shown in the supplementary section Supplementary Note 7 and Supplementary Fig. S6. A striking difference between the two sets of images in Fig. 5 is that skyrmionic bubbles are formed in the pre-cooling phase, but stripe domains form in the post-cooling phase, under otherwise equivalent circumstances. Since magnetic skyrmions predominantly form when an external field close to the saturation field is applied, this suggests that the saturation field of our sample has increased during the phase transition to the post-cooling phase. This could be explained by an increase in the magnetization in the post-cooling state, as this would mean that the dipolar energy is still large relative to the external field contribution. Magnetometry measurements of a bulk sample using a SQUID support this idea, and yield larger magnetizations

at moderate fields in the post-cooling phase compared to the pre-cooling phase, as discussed earlier in this subsection.

Magnetic ordering. It was shown in the previous subsection that Fe_5GeTe_2 shows a decrease in magnetization upon cooling from T_{C2} down to T_S while the sample is in the metastable pre-cooling phase (see Fig. 3), which indicates that Fe_5GeTe_2 might exhibit ferrimagnetic order or is in a spin glassy state. To distinguish these effects, we study next whether or not Fe_5GeTe_2 is in a glassy spin state. To this end, the micromagnetic anisotropy constant K is experimentally determined in two independent ways and compared. One method is to consider the hard-axis saturation field $B_{\text{sat}}^{\text{IP}}$, which is simply related to the exchange constant via the Stoner-Wohlfarth model³². By finding the total energy minimum with a given field applied along the hard-axis, and including Zeeman and anisotropy interactions, one finds that the expression for in-plane saturation is:

$$K_{\text{IP}} = B_{\text{sat}}^{\text{IP}} \frac{M_s}{2}. \quad (4)$$

A complementary approach to determine K is via the domain wall width δ ³³:

$$\delta = \pi \Delta = \pi \sqrt{\frac{A}{K_\delta}}, \quad (5)$$

where A is the micromagnetic exchange constant and Δ is a fit parameter used in the determination of the domain wall width δ from the measured domain wall profile. Note that when measuring K_{IP} , the quantities involved are determined on a macroscopic scale, whereas the determination of K_δ will require knowledge of the exchange interaction, which is short-ranged and dominates on the nanoscale. Thus, local disorder present in spin glasses³⁴ would manifest itself by affecting K_δ and K_{IP} differently and leading to different values. Consequently, if K_δ and K_{IP} are consistent with each other, Fe_5GeTe_2 is not in a spin glassy state.

To obtain K_δ , the micromagnetic exchange coupling constants were calculated using the JuKKR density functional theory (DFT) code³⁵ (see the Methods section). This code employs the method of infinitesimal rotations^{36–38} to map the interactions among

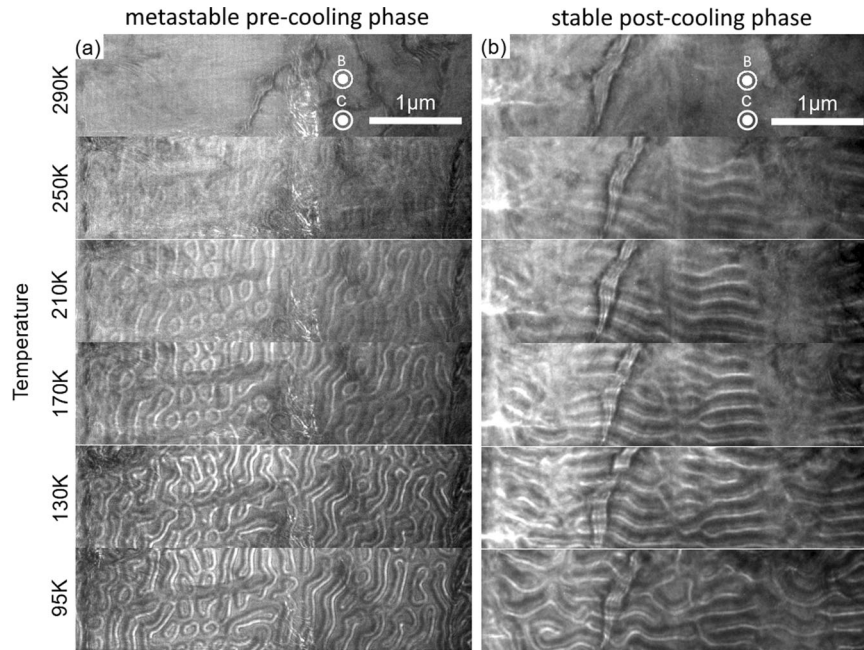


Fig. 5 Fresnel images of Fe_5GeTe_2 at various temperatures. The temperature is indicated in the figure and a constant external field of $B = 100$ mT is applied. A defocus of -1 mm was used in a plan-view lamella (c-axis is perpendicular to the image plane), recorded before **a** and after **b** leaving the sample in liquid nitrogen for one hour.

spins $\vec{S}_i = \vec{M}_i/\mu_i$ ($\mu_i = |\vec{M}_i|$) at lattice sites i onto the extended classical Heisenberg Hamiltonian

$$H = -\sum_{i \neq j} J_{ij} (\vec{S}_i \cdot \vec{S}_j) - \sum_{i \neq j} \vec{D}_{ij} \cdot (\vec{S}_i \times \vec{S}_j) - \sum_i K (\vec{S}_i \cdot \hat{e}_z)^2, \quad (6)$$

where the first term describes the exchange interaction, the second term represents DMI, and the final term describes the uniaxial out-of-plane anisotropy. The micromagnetic spin stiffness is

$$A = \frac{1}{2V} \sum_{i \neq j} J_{ij} \vec{r}_{ij}^2, \quad (7)$$

where V is the volume per Fe atom, which can be calculated from the exchange coupling constants³⁷. These parameters define the micromagnetic energy functional

$$E[\vec{m}] = \int d\vec{r} [A(\nabla \vec{m})^2 + Km_z^2], \quad (8)$$

where the contribution of the spiralization that is related to the DMI vectors is neglected because it is found to vanish. The micromagnetic exchange constant obtained from this method is

$$A_{\text{DFT}} = 0.1508 \text{ eV nm}^{-1}. \quad (9)$$

An alternative, independent method to approximate the micromagnetic exchange constant A by considering the magnetic ordering temperature and crystal structure, is presented and executed in section Supplementary Note 3 of the supplementary information. The result is $A_{\text{H}} = (0.060 \pm 0.007) \text{ eV nm}^{-1}$ and it is fairly close to the DFT value considering that many assumptions are made in this alternative method. Further calculations and comparisons to experiment, which support the DFT models and calculations are presented in the supplementary sections Supplementary Note 4 and Supplementary Note 5.

To determine the effective anisotropy K_δ using the spin stiffness A , we next need to determine the domain wall width δ . The domain wall parameter Δ can in principle be determined from phase shift images obtained using off-axis electron holography by fitting the

magnetic phase gradient profile perpendicular to a domain wall. Whereas Fresnel images would introduce problems in the accurate determination of the domain wall profiles due to their necessary defocus, off-axis electron holography images are in-focus and as such allow one to extract the domain wall profiles directly. The profile can then immediately be fit to the well-known theoretical domain wall profile $M_z^{\text{theo}}(x) = M_0 \cdot \tanh(x/\Delta)$. In reality the profiles will not be perfectly centered, so we use a fit function which allows for shifts:

$$M_z^{\text{fit}}(x) = M_0 \cdot \tanh((x - x_{\text{shift}})/\Delta) + M_{\text{shift}}, \quad (10)$$

where M_0 is the amplitude of the magnetization, x is the position perpendicular to the domain wall, and x_{shift} and M_{shift} are the free fit parameters accounting for imperfect centering. To obtain reliable results, each line drawn perpendicular to the domain walls has a width of 277.5 nm (300 pixels) to average across. An example of such a line is shown in Fig. 6(a), and the corresponding magnetic profile and fit is shown in panel (b). Overall, the domain wall width has been determined via four independent lines at 95 K and five different lines at 200 K. The resulting domain wall widths are $\delta^{95\text{K}} = (24.2 \pm 5.2) \text{ nm}$ and $\delta^{200\text{K}} = (36.3 \pm 3.5) \text{ nm}$. The uncertainties are estimated via the standard deviation of the domain wall widths obtained from all lines used at each temperature. Accordingly, the fit parameters are $\Delta = \delta/\pi$. These experimental domain wall widths are in line with results from a DFT calculation evaluated in the supplementary section Supplementary Note 5. The corresponding results are shown in Supplementary Fig. S3 and Supplementary Fig. S4. Thus, all required parameters to find K_δ via equation (5) are known, and we find using A_{DFT} and the parameters Δ :

$$K_\delta^{95\text{K}} = (2.55 \pm 0.55) \cdot 10^{-3} \text{ eV nm}^{-3}, \quad (11)$$

$$K_\delta^{200\text{K}} = (1.13 \pm 0.11) \cdot 10^{-3} \text{ eV nm}^{-3}. \quad (12)$$

For the alternative determination of the anisotropy via the saturation field along the hard-axis K_{IP} , images of the cross-

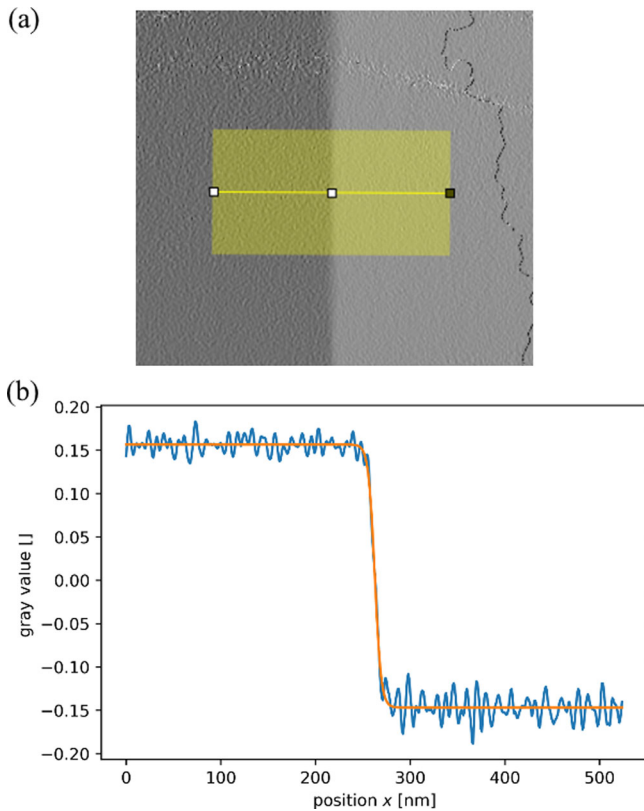


Fig. 6 Analysis of the magnetic contrast of a magnetic domain wall, with the aim to determine the domain wall width. **a** Magnetic phase gradient image obtained using off-axis electron holography. A profile was extracted in the direction perpendicular to a 180° domain wall along the wide line. **b** Phase gradient profile (blue) and corresponding fit (orange). This example shows one magnetic profile across a domain wall at 95 K. Error bars are omitted for readability; the standard deviation of each measured gray value is 0.009.

section lamella sample are recorded at various field strengths at 95 K and 200 K (examples of images at 95 K are shown in Supplementary Fig. S1(c–e) in the supplementary information). The point at which the magnetic contrast completely vanishes as a function of magnetic field is approximated by splining the data for which there is magnetic contrast, and interpolating to the point where the minority domain has a width of zero. It should be noted that, since the field may not be applied perfectly perpendicular to the *c*-axis, this field is the monodomainization field, and serves as a lower bound for the hard-axis saturation field. However, it can be used as an estimation for the hard-axis saturation field. In this case, the saturation fields are estimated to be $B_{\text{sat}}^{\text{IP},95\text{K}} = (285 \pm 85) \text{ mT}$ and $B_{\text{sat}}^{\text{IP},200\text{K}} = (143 \pm 43) \text{ mT}$. Accordingly, in conjunction with the saturation magnetization M_s from the SQUID measurements and inserting into equation (4), the micromagnetic anisotropy constants from this method are evaluated to be

$$K_{\text{IP}}^{95\text{K}} = (0.72 \pm 0.22) \cdot 10^{-3} \text{ eV nm}^{-3}, \quad (13)$$

$$K_{\text{IP}}^{200\text{K}} = (0.36 \pm 0.11) \cdot 10^{-3} \text{ eV nm}^{-3}. \quad (14)$$

Finally, the anisotropy constants obtained via both the domain wall and hard-axis saturation method can be compared. At 95 K the ratio between the effective anisotropy constants is $K_{\delta}^{95\text{K}}/K_{\text{IP}}^{95\text{K}} = 3.53 \pm 1.30$, and at 200 K it is $K_{\delta}^{200\text{K}}/K_{\text{IP}}^{200\text{K}} = 3.11 \pm 0.98$. Thus, the two methods to determine K used in this work, although they are completely independent and cover vastly

different length scales, yield results which are on the same order of magnitude. The fact that the ratio K_{δ}/K_{IP} may systematically be larger than 1 could be attributed to the fundamental approximations used. Namely, since the hard-axis saturation field will be slightly larger than the monodomainization field, which we used to estimate the saturation field, K_{IP} should in reality be systematically slightly larger than the values we obtained. If the obtained anisotropy constants would differ by a large margin one could suggest that the material might be in a spin glassy state. But since they do not differ greatly, this analysis implies that the material is not in a spin glassy state. As such, this analysis in conjunction with the SQUID results indicates that Fe_5GeTe_2 might not be in a spin glassy state, but in a ferrimagnetic state while it is in the pre-cooling phase, as previously claimed^{28,29}.

Conclusions

In conclusion, we have presented experimental observations of spin structures and determined magnetic properties in the promising 2D vdW magnet Fe_5GeTe_2 , to understand the magnetic ordering of this material. Non-chiral magnetic skyrmions form in the material near room temperature when magnetic fields close to the saturation field are applied. The achirality of these magnetic bubbles suggests that there is no considerable bulk DMI present in Fe_5GeTe_2 , which in turn supports the conclusion that Fe_5GeTe_2 exhibits an underlying centrosymmetry, in line with the reported $R\bar{3}m$ crystal structure, rather than the otherwise proposed non-centrosymmetric $R3m$ crystal structure. Furthermore, the observed magnetic bubbles are Bloch-type bubbles, which suggests that there is no significant interfacial DMI in our samples either. Future studies on Fe_5GeTe_2 heterostructures, which induce the formation of Néel-type bubbles due to interfacial DMI are feasible¹⁶. Since Fe_5GeTe_2 exhibits a lower magnetization in the pre-cooling phase than in the post-cooling phase, we were able to observe bubbles at lower fields and down to zero external field in the pre-cooling phase compared to the post-cooling phase. Furthermore, by considering the anisotropy constants obtained via two independent methods, namely via the hard-axis saturation field and via the domain wall profile and predicted exchange constants, we conclude that Fe_5GeTe_2 is not in a spin glassy state. However, a significant drop of the magnetization with decreasing temperature observed in SQUID measurements suggests that Fe_5GeTe_2 is a ferrimagnet instead of a simple ferromagnet whilst in the pre-cooling phase. Future neutron diffraction experiments are required to fully ascertain the spin structure of Fe_5GeTe_2 . We have thus completed the necessary steps toward room temperature spintronics devices based on skyrmion type spin structures, which are of significant interest for novel information storage and non-conventional computing concepts using 2D magnets.

Methods

A. Crystal synthesis. Single crystals of Fe_5GeTe_2 with an average size of $2 \times 2 \times 0.5 \text{ mm}^3$ were synthesized in quartz glass ampoules from the elements Fe, Ge, and Te in a 6 : 1 : 2 ratio in the presence of iodine as mineralizer. Similar to reference⁴, Ge was supplied as a powder on the bottom of the quartz glass tube. Fe and Te were pressed to separate pellets of 1 mm diameter and positioned on top of the Ge powder without direct contact between the pellets. The reaction thus predominantly occurs through the gas phase and increases the single crystal size to several millimeters. The vacuum-sealed ampoules were heated up to 750 °C with 120 K/h and kept at this temperature for about 2 weeks before quenching them in room temperature water. The composition of the single crystals was confirmed by energy dispersive X-ray spectroscopy (Tescan SEM Vega TS 5130 MM equipped with a silicon drift detector, Oxford) with a ratio of Fe : Ge : Te of 4.72(5) : 1 : 1.94(4).

B. Lamella preparation. Electron transparent cross-section and plan-view lamellae were prepared using a 30 kV Ga^+ focused ion beam and scanning electron

microscope (FIB-SEM) FEI Helios platform. The energy of the ion beam was decreased to 5 kV in the last steps of the thinning to minimize surface damage.

C. Transmission electron microscopy. Scanning transmission electron microscopy (STEM) and energy dispersive X-ray (EDX) spectroscopy were carried out using an FEI Titan TEM equipped with a Schottky field emission gun operated at 200 kV, a CEOS probe aberration corrector, a high angle annular dark-field detector (HAADF) and a Super-X EDX detection system³⁹. Composition maps were obtained using the Thermo Fisher Scientific Velox software.

Magnetic imaging was carried out using Fresnel defocus and off-axis electron holography in an FEI Titan TEM equipped with a Schottky field emission gun, a CEOS image aberration corrector, a post-specimen electron biprism and a 4k × 4k Gatan K2-IS direct detection camera⁴⁰. A liquid-nitrogen-cooled specimen holder (Gatan model 636) was used to vary the sample temperature. The microscope was operated at 300 kV in magnetic field-free conditions (Lorentz mode) by using the first transfer lens of the aberration corrector as the primary imaging lens. The conventional objective lens was used to apply the chosen magnetic fields to the sample, which were pre-calibrated using a Hall probe. The field is applied along the electron beam direction i.e., perpendicular to the sample plane. For off-axis electron holography, the electron biprism was used to overlap a reference wave travelling in vacuum with an object wave passing through the sample. An elliptical illumination was used to optimize the coherence of the beam in the direction perpendicular to the biprism. The hologram width was 2.7 μm and the fringe spacing was 2.5 nm. Magnetic induction maps were reconstructed using Fourier transforms with the Holoworks plugin in the Digital Micrograph software (Gatan)⁴¹. The contribution of the mean inner potential to the phase was removed by subtracting the phase of an hologram acquired above the Curie temperature.

D. DFT atomistic exchange tensor calculations. We performed density functional theory (DFT) calculations for bulk Fe₅GeTe₂ using the experimental lattice constants, $a = 4.04(2)\text{Å}$, $c = 29.19(3)\text{Å}$, from May et al.⁴. In order to account for the two Fe atoms at 50% occupancy we employed the use of the coherent potential approximation (CPA)⁴². We perform our calculations with the JuKKR code³⁵ which implements the full potential Korringa Kohn Rostoker (KKR) Green's Function method⁴² with an exact description of the shape of the atomic cell^{43,44}. We use an angular momentum cutoff $l_{\text{max}} = 3$ and a generalised gradient approximation (GGA) to obtain the exchange-correlation potential⁴⁵. Our calculations of the exchange coupling constants for the determination of the atomistic spin stiffness are based on the model of infinitesimal rotations^{36,37}. The domain wall widths calculated in the supplementary section Supplementary Note 5 are determined using the Spirit code⁴⁶. The calculations are orchestrated through the AiiDA framework⁴⁷ via the AiiDA-KKR⁴⁸ and AiiDA-Spirit⁴⁹ plugins.

Data availability

All data used in the present work are available upon reasonable request.

Code availability

The DFT and spin dynamics codes JuKKR (<https://iffgit.fz-juelich.de/kkr/jukkr>) and Spirit (<https://github.com/spirit-code/spirit>) are open-source software packages which were used through the AiiDA-KKR (<https://github.com/JuDFTEam/aaida-kkr>) and AiiDA-Spirit (<https://github.com/JuDFTEam/aaida-spirit>) python interfaces, respectively. Additional code used in the present work is available upon reasonable request.

Received: 21 May 2022; Accepted: 3 October 2022;

Published online: 18 October 2022

References

- Gibertini, M., Koperski, M., Morpurgo, A. F. & Novoselov, K. S. Magnetic 2d materials and heterostructures. *Nat. Nanotechnol.* **14**, 408–419 (2019).
- Huang, B. et al. Layer-dependent ferromagnetism in a van der Waals crystal down to the monolayer limit. *Nature* **546**, 270–273 (2017).
- Deng, Y. et al. Gate-tunable room-temperature ferromagnetism in two-dimensional Fe₃GeTe₂. *Nature* **563**, 94–99 (2018).
- May, A. F. et al. Ferromagnetism near room temperature in the cleavable van der Waals crystal Fe₅GeTe₂. *ACS Nano* **13**, 4436–4442 (2019).
- Zhang, H. et al. Itinerant ferromagnetism in van der Waals Fe_{5-x}GeTe₂ crystals above room temperature. *Phys. Rev. B* **102**, 064417 (2020).
- Ershadrad, S., Ghosh, S., Wang, D., Kvashnin, Y. & Sanyal, B. Unusual magnetic features in two-dimensional Fe₅GeTe₂ induced by structural reconstructions. *J. Phys. Chem. Lett.* **13**, 4877–4883 (2022).
- May, A. F., Du, M.-H., Cooper, V. R. & McGuire, M. A. Tuning magnetic order in the van der Waals metal Fe₅GeTe₂ by cobalt substitution. *Phys. Rev. Mater.* **4**, 074008 (2020).
- Zhang, H. et al. A room temperature polar magnetic metal. *Phys. Rev. Mater.* **6**, 044403 (2022).
- Zhang, H. et al. Room-temperature skyrmion lattice in a layered magnet (Fe_{0.5}Co_{0.5})₅GeTe₂. *Sci. Adv.* **8**, eabm7103 (2022).
- Pei, K. et al. Controllable domain walls in two-dimensional ferromagnetic material Fe₃GeTe₂ based on the spin-transfer torque effect. *ACS Nano* **15**, 19513–19521 (2021).
- Purbawati, A. et al. In-plane magnetic domains and néel-like domain walls in thin flakes of the room temperature CrTe₂ van der Waals ferromagnet. *ACS Appl. Mater. Interfaces* **12**, 30702–30710 (2020).
- Fert, A., Reyren, N. & Cros, V. Magnetic skyrmions: advances in physics and potential applications. *Nat. Rev. Mater.* **2**, 17031 (2017).
- Everschor-Sitte, K., Masell, J., Reeve, R. M. & Kläui, M. Perspective: Magnetic skyrmions—overview of recent progress in an active research field. *J. Appl. Phys.* **124**, 240901 (2018).
- Tokura, Y. & Kanazawa, N. Magnetic skyrmion materials. *Chem. Rev.* **121**, 2857–2897 (2021).
- Ding, B. et al. Observation of magnetic skyrmion bubbles in a van der Waals ferromagnet Fe₃GeTe₂. *Nano Lett.* **20**, 868–873 (2020).
- Peng, L. et al. Tunable néel-bloch magnetic twists in Fe₃GeTe₂ with van der Waals structure. *Adv. Funct. Mater.* **31**, 2103583 (2021).
- Gao, Y. et al. Spontaneous (anti)meron chains in the domain walls of van der Waals ferromagnetic Fe_{5-x}GeTe₂. *Adv. Mater.* **32**, 2005228 (2020).
- May, A. F., Bridges, C. A. & McGuire, M. A. Physical properties and thermal stability of Fe_{5-x}GeTe₂ single crystals. *Phys. Rev. Mater.* **3**, 104401 (2019).
- Stahl, J., Shlaen, E. & Johrendt, D. The van der Waals ferromagnets Fe_{5-d}GeTe₂ and Fe_{5-d-x}Ni_xGeTe₂ - crystal structure, stacking faults, and magnetic properties. *Z. Anorg. Allg. Chem.* **644**, 1923–1929 (2018).
- Li, Z. et al. Magnetic critical behavior of the van der Waals Fe₅GeTe₂ crystal with near room temperature ferromagnetism. *Sci. Rep.* **10**, 15345 (2020).
- Manchon, A. & Belabbes, A. Spin-orbitronics at transition metal interfaces. *Solid State Phys.* **68**, 1–89 (2017).
- Loudon, J. C. et al. Do images of biskyrmions show Type-II Bubbles? *Adv. Mater.* **31**, e1806598 (2019).
- Yokota, T. Numerical investigation of magnetic bubble types in a two-dimensional ferromagnetic system with dipole–dipole interactions. *J. Phys. Soc. Jpn.* **88**, 084702 (2019).
- Leonov, A. O. & Kézsmárki, I. Skyrmion robustness in noncentrosymmetric magnets with axial symmetry: The role of anisotropy and tilted magnetic fields. *Phys. Rev. B* **96**, 214413 (2017).
- Lemesh, I. et al. Current-induced skyrmion generation through morphological thermal transitions in chiral ferromagnetic heterostructures. *Adv. Mater.* **30**, e1805461 (2018).
- Woo, S. et al. Observation of room-temperature magnetic skyrmions and their current-driven dynamics in ultrathin metallic ferromagnets. *Nat. Mater.* **15**, 501–506 (2016).
- Mathieu, R., Jönsson, P., Nam, D. N. H. & Nordblad, P. Memory and superposition in a spin glass. *Phys. Rev. B* **63**, 092401 (2001).
- Alahmed, L. et al. Magnetism and spin dynamics in room-temperature van der Waals magnet Fe₅GeTe₂. *2D Mater.* **8**, 045030 (2021).
- Ohta, T. et al. Enhancement of coercive field in atomically-thin quenched Fe₅GeTe₂. *Appl. Phys. Express* **13**, 043005 (2020).
- Johansen, T. H., Pan, A. V. & Galperin, Y. M. Exact asymptotic behavior of magnetic stripe domain arrays. *Phys. Rev. B* **87**, 060402 (2013).
- De Teresa, J. M. et al. Spin-Glass Insulator State in (Tb-La)_{2/3}Ca_{1/3}MnO₃ Perovskite. *Phys. Rev. Lett.* **76**, 3392–3395 (1996).
- Stoner, E. C. & Wohlfarth, E. A mechanism of magnetic hysteresis in heterogeneous alloys. *Philos. Trans. R. Soc. A* **240**, 599–642 (1948).
- Heide, M., Bihlmayer, G. & Blügel, S. Dzyaloshinskii-Moriya interaction accounting for the orientation of magnetic domains in ultrathin films: Fe/W(110). *Phys. Rev. B* **78**, 140403 (2008).
- Sherrington, D. & Kirkpatrick, S. Solvable model of a spin-glass. *Phys. Rev. Lett.* **35**, 1792–1796 (1975).
- The JuKKR developers. The Jülich KKR Codes (2021). <https://jukkr.fz-juelich.de>.
- Liechtenstein, A., Katsnelson, M., Antropov, V. & Gubanov, V. Local spin density functional approach to the theory of exchange interactions in ferromagnetic metals and alloys. *J. Magn. Magn. Mater.* **67**, 65–74 (1987).
- Schwefflinghaus, B., Zimmermann, B., Heide, M., Bihlmayer, G. & Blügel, S. Role of Dzyaloshinskii-Moriya interaction for magnetism in transition-metal chains at Pt step edges. *Phys. Rev. B* **94**, 024403 (2016).
- Ebert, H. & Mankovsky, S. Anisotropic exchange coupling in diluted magnetic semiconductors: Ab initio spin-density functional theory. *Phys. Rev. B* **79**, 045209 (2009).

39. Kovács, A., Schierholz, R. & Tillmann, K.FEI Titan G2 80-200 CREWLEY. Journal of large-scale research facilities JLSRF 2 (2016). <https://doi.org/10.17815/jlsrf-2-68>.
40. Boothroyd, C., Kovács, A. & Tillmann, K.FEI Titan G2 60-300 HOLO. Journal of large-scale research facilities JLSRF 2 (2016). <https://doi.org/10.17815/jlsrf-2-70>.
41. Völkl, E., Allard, L. F. & Frost, B. A software package for the processing and reconstruction of electron holograms. *J. Microsc.* **180**, 39–50 (1995).
42. Ebert, H., Ködderitzsch, D. & Minár, J. Calculating condensed matter properties using the KKR-Green's function method - Recent developments and applications. *Rep. Prog. Phys.* **74**, 096501 (2011).
43. Stefanou, N., Akai, H. & Zeller, R. An efficient numerical method to calculate shape truncation functions for Wigner-Seitz atomic polyhedra. *Comput. Phys. Commun.* **60**, 231–238 (1990).
44. Stefanou, N. & Zeller, R. Calculation of shape-truncation functions for Voronoi polyhedra. *J. Phys. Condens. Matter* **3**, 7599–7606 (1991).
45. Perdew, J. P., Burke, K. & Ernzerhof, M. Generalized gradient approximation made simple. *Phys. Rev. Lett.* **77**, 3865–3868 (1996).
46. Müller, G. P. et al. Spirit: Multifunctional framework for atomistic spin simulations. *Phys. Rev. B* **99**, 224414 (2019).
47. Huber, S. P. et al. AiiDA 1.0 a scalable computational infrastructure for automated reproducible workflows and data provenance. *Sci. Data* **7**, 300 (2020).
48. Rießmann, P., Bertoldo, F. & Blügel, S. The AiiDA-KKR plugin and its application to high-throughput impurity embedding into a topological insulator. *npj Comput. Mater.* **7**, 13 (2021).
49. Rießmann, P. et al. The AiiDA-Spirit Plugin for Automated Spin-Dynamics Simulations and Multi-Scale Modeling Based on First-Principles Calculations. *Front. Mater.* **9**, 825043 (2022).

Acknowledgements

The work at JGU Mainz was funded by the Deutsche Forschungsgemeinschaft (DFG, German Research Foundation)—TRR 173/2—268565370 (projects A01 and B02), project 403502522 (SPP 2137 skyrmionics) the EU (FET-Open grant agreement no. 863155 (s-Nebula)), and the Research Council of Norway (QuSpin Center 262633). The work at JGU Mainz and FZJ was funded by ERC Synergy grant agreement no. 856538 (3D MAGiC), T.S., P.R., S.B. and Y.M. gratefully acknowledge the Jülich Supercomputing Centre for providing computational resources and Deutsche Forschungsgemeinschaft (DFG, German Research Foundation)—TRR 173/2 - 268565370 (project A11), TRR 288 - 422213477 (project B06). T.G.S. would like to thank Dr. Sarah Jenkins, Dr. Dongwook Go and Dr. Fabian Lux for fruitful discussions. We are grateful for computing time granted by the JARA Vergabegremium and provided on the JARA Partition part of the supercomputer CLAIx at RWTH Aachen University (project number jara0191). The work at FZJ was furthermore funded by the Deutsche Forschungsgemeinschaft (DFG, German Research Foundation) under Germany's Excellence Strategy – Cluster of Excellence Matter and Light for Quantum Computing (ML4Q) EXC 2004/1 – 390534769, and we thank the Bavarian Ministry of Economic Affairs, Regional Development and Energy for financial support within High-Tech Agenda Project “Bausteine für das Quantencomputing auf Basis topologischer Materialien mit experimentellen und theoretischen Ansätzen”.

Author contributions

Tanja Scholz synthesized all Fe_5GeTe_2 samples used in the present work. Thibaud Denneulin prepared the TEM lamellae and conducted the LTEM experiments with the

help of Amir Tavabi. András Kovács carried out the STEM and EDX measurements. Aga Shahee conducted the SQUID and X-ray diffraction measurements. Tom G. Saunderson and Philipp Rießmann contributed equally to the DFT results. Martin Gradhand and Phivos Mavropoulos helped with the determination of the spin stiffness via T_C . Phivos Mavropoulos provided the theoretical T_C of Fe_5GeTe_2 based on DFT results. Maurice Schmitt analyzed the experimental and theoretical results to yield insights into the spin ordering of Fe_5GeTe_2 , and wrote the paper with Mathias Kläui. Bettina Lotsch supervised the synthesis of the Fe_5GeTe_2 crystals. Yuriy Mokrousov and Stefan Blügel discussed and supervised the DFT work. Rafal Dunin-Borkowski supervised the microscopy work. Mathias Kläui supervised the experimental SQUID measurements and devised the study. All authors commented on the results and contributed to the manuscript.

Funding

Open Access funding enabled and organized by Projekt DEAL.

Competing interests

The authors declare no competing interests.

Additional information

Supplementary information The online version contains supplementary material available at <https://doi.org/10.1038/s42005-022-01031-w>.

Correspondence and requests for materials should be addressed to Mathias Kläui.

Peer review information *Communications Physics* thanks Hongrui Zhang, Zhenxiang Cheng and the other, anonymous, reviewer(s) for their contribution to the peer review of this work. Peer reviewer reports are available.

Reprints and permission information is available at <http://www.nature.com/reprints>

Publisher's note Springer Nature remains neutral with regard to jurisdictional claims in published maps and institutional affiliations.



Open Access This article is licensed under a Creative Commons Attribution 4.0 International License, which permits use, sharing, adaptation, distribution and reproduction in any medium or format, as long as you give appropriate credit to the original author(s) and the source, provide a link to the Creative Commons license, and indicate if changes were made. The images or other third party material in this article are included in the article's Creative Commons license, unless indicated otherwise in a credit line to the material. If material is not included in the article's Creative Commons license and your intended use is not permitted by statutory regulation or exceeds the permitted use, you will need to obtain permission directly from the copyright holder. To view a copy of this license, visit <http://creativecommons.org/licenses/by/4.0/>.

© The Author(s) 2022